

Piezoelectric Soft Robot Inchworm Motion by Controlling Ground Friction through Robot Shape

Zhiwu Zheng, Prakhar Kumar, Yenan Chen, Hsin Cheng,
Sigurd Wagner, Minjie Chen, Naveen Verma and James C. Sturm

Abstract—Electrically driven soft robots enable small and light bodies, as well as environmental compatibility, various locomotion, and safe operation. In particular, electrostatic actuators (for example, piezoelectric actuators) are fast responded. However, scalable ways for seamless integration and untethered operation remain unclear. In addition, soft body nature modeling, including environmental interactions, is a long-standing challenge. Furthermore, more locomotion mechanisms need to be explored. In this paper, we have designed, modeled, and demonstrated a soft robot that, for the first time, starts to address all these questions. It has a linear array of five actuators in a planar structure, opening doors for integration and free operation. A new inchworm-inspired crawling motion mechanism was designed and validated by relying on posture self-adjustment. The first analytical soft body model including piezoelectricity, gravity, and ground interactions that well explain robot locomotion was developed and validated by experiments. We demonstrated the robot's forward and backward motion and explored the effects of payload and driving speed: 1207 μm movement per cycle and up to 200 g payload (16x body weight) can be carried while moving. This work paves the way for fast-responding robots in complicated unknown environments.

Index Terms—Soft robotics, piezoelectric actuators, soft body model, inchworm, large-area electronics

I. INTRODUCTION

SOFT robots have drawn broad interest due to their “soft” nature enabling safe human-robot interactions and great environmental compatibility, unlike their rigid counterparts featured by great power and high stiffness. While most soft robots are driven by pneumatic power [1]. Electrostatic soft robots, made of piezoelectric actuators for example, may be easier to integrate [2], less bulky, faster to respond (driving frequency usually hundreds or a few kilo Hz [3], [4]), lighter, and even microscale [5].

There are various bioinspired soft robots. Examples include robotic fish [6], squid [7], bees [5], octopuses [8], and inchworms [9], [10], [11], [12], [13], [14], [15]. An inchworm has a soft body by nature. Our robot design in this work is analogous to an inchworm. The key to its motion is to have an alternating end of the body fixed on the ground while moving the other end. Its motion cycle involves first raising its midsection while holding its front legs fixed on a surface, causing its back end

This work was supported by the Semiconductor Research Corporation (SRC), DARPA, Princeton Program in Plasma Science and Technology, and Princeton University. (*Corresponding author:* Zhiwu Zheng)

The authors are with the Department of Electrical and Computer Engineering, Princeton University, Princeton, New Jersey 08544, U.S.A. (e-mail: zhiwuz@princeton.edu; prakhark@princeton.edu; yenanc@princeton.edu; hsin@princeton.edu; wagner@princeton.edu; minjie@princeton.edu; nverma@princeton.edu; sturm@princeton.edu).

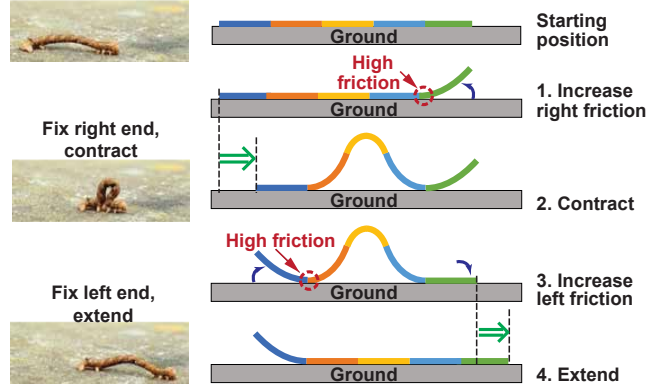


Figure 1. Inchworm motion and analogous robot motion of “contract” and “extend” cycles in 4 steps. The robot consists of five thin-film piezoelectric actuators (each a different color) on a common substrate. Raising the actuator on one end increases the friction on that end relative to the opposite end.

to move forward towards the head. (Fig. 1). In a second step, it fixes its rear legs to the surface and extends its front end forward. There are various kinds of bioinspired mechanisms to do that [16]. This includes attaching frictional films to the ends and putting one of the frictional ends down to hold on the ground [10], [11]. Alternative extra films include using anisotropic friction pads [9], [12], passive or electro-active adhesives [14], [15], [17], or magnets [13]. Sharp hooks [18] or asymmetric feet [19] are also used for this anchoring crawling motion.

Research opportunities are open for exploring new ways to hold a desired end fixed. In this paper, we describe a new mechanism for holding with the effect of a robot’s posture on ground force and friction difference, validate the new principle by model and experiment.

Our soft-robot design is implemented with five piezoelectric actuators on a single substrate, where the central three actuators cause the central section to lift off the ground and thus contract and expand in a lateral direction. Thus, whereas an inchworm holds its desired end fixed by “sticky” feet, our soft robot holds the desired end fixed by increasing the relative friction to the ground of one end of the robot vs. the other.

This paper will show that the gravitational force of the robot on the ground (referred to as the “ground force”) on one end vs. the other can be increased by lifting the head or tail off of the ground using the 1st or 5th piezoelectric actuator. This then leads to an asymmetry in friction on one end vs. the other, analogous to the inchworm’s ability to choose which end has “sticky feet” (Fig. 1).

The paper has three parts:

- 1) We develop an analytical model of the robot's shape as a function of the voltages on the piezoelectrics, including the effect of gravity on the shape. The model is compared to experiments using commercially-available piezoelectric actuators [20].
- 2) We analytically derive the difference in the force between the robot and the ground on one end vs. the other as a function of piezoelectric voltages on either end and experimentally validate it.
- 3) With the resulting asymmetry in friction between the two ends, we experimentally demonstrate the forward and reverse motion of the robot, including the ability to carry a payload.

II. ROBOT DESIGN AND CONSTRUCTION

Each actuator of Fig. 1 is realized with a thin-film PZT fiber composite bonded to a thin ($50\text{ }\mu\text{m}$) steel substrate with $100\text{ }\mu\text{m}$ of epoxy. In practice, applying positive/negative voltages cause the piezoelectric material to expand/contract laterally, causing the assemble to curl up/down (Fig. 2). We used commercially available piezoelectric fiber composite (Smart Material Corp., Sarasota, Florida. Part numbers: M-8514-P1, M-8514-P2).

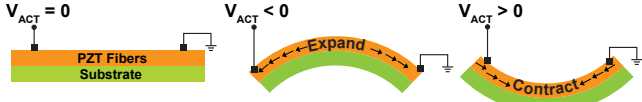


Figure 2. Mechanism of bending. The unit curves down (up) with contraction (extension) of the piezoelectric actuator under positive (negative) voltage.

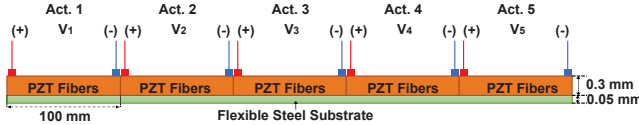


Figure 3. Cross-section of a five-actuator soft robot prototype, 500 mm long and 20 mm wide. Each unit includes a piezoelectric unit made of a lead zirconate titanate (PZT) fiber composite, controlled by voltage signals wired from off-robot voltage supplies. All the units share a common steel foil substrate.

Five fiber units were laminated onto a single steel foil ($2.5\text{ cm} \times 50\text{ cm}$) to create the robot (Fig. 3). In practice, the actuator degrades if a significant voltage is applied in the direction other than designed. Thus, we designed our robot to rely on one sign of voltage in each actuator, extend or contract, so that each actuator bends either up or down, but not both. Since all actuators were on top of the substrate, the contracted piezoelectric unit (#3, in Fig. 3) is applied negative voltages in normal operations and bend down, while the others (#1, #2, #4, #5) are applied positive voltages and bend up.

Fig. 4a shows the top view of the robot experimental setup, and Fig. 4b shows the side view when it is actuated. Thin and light gold wires are connected from the solder pads on the actuators to high voltage supplies.

III. SOFT BODY ROBOT MODEL

Realizing this inchworm concept relies on alternating raising the friction of the robot with the ground on the left and then the right end of the robot. Predicting this friction requires knowledge of the exact shape of the robot, including the effects of gravity on the shape. Also critical is the profile of the vertical force between the actuator and the ground (which we refer to as "ground force" distribution).

This section develops an analytical static model of the robot and ground force distribution as a function of applied voltages on the actuators.

A. Previous work

Precise analytical modeling is the key to the design and control of the robot. Challenges are caused by the soft body nature and its complex interaction with the environment. Current methods of modeling a piezoelectric soft robot are usually constant-curvature models [21], [22], [23] and pseudo rigid body models [24], [25], [26]. The constant-curvature model treats an actuator (or part of it) as a perfect arc with some radius, and then coordinate transformation can be used to form the kinematics of the robot similar to a rigid robot. Pseudo rigid body model, as an alternative way, treats the robot as joints connected by short links and then treats it as a rigid robot. Research works on soft-body-based models are open. There is research to include only the gravity loading by applying Cosserat rod theory to a continuum robot in a cantilever case [27].

In this paper, we are going to develop a soft-body-based model for our robot. It will also include the robot's interaction with the ground – the vertical force exerted on the robot as of the gravity (referred to "ground force" later) and frictions. They usually have tremendous effects on the shape of the robot as of the body's elasticity.

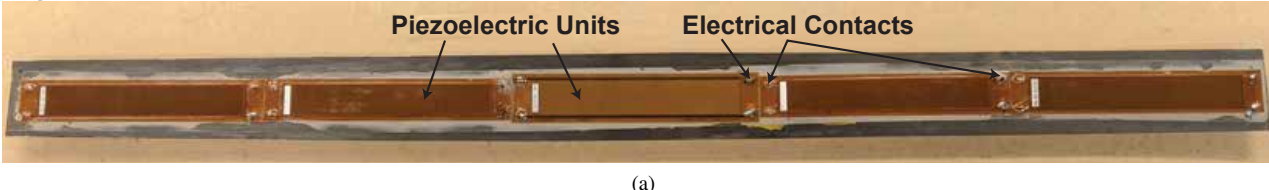
B. Soft robot shape modeling

1) Summary of the model: When voltages are applied to the actuators, some parts of the robot will be flat on the ground, and the other parts will lift off. In this section, we develop a model that predicts the shape considering gravity. Without gravity, the shape in each section is simply determined by piezoelectricity. The key property of the model is a self-consistent approach to determine which part of the robot is suspended.

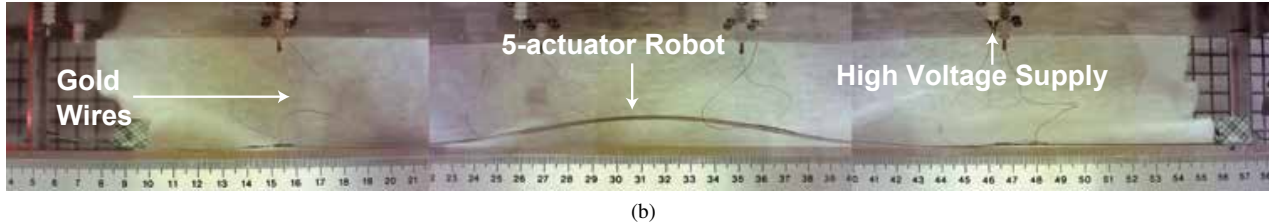
We applied the model to different scenarios: a single actuator clamped on the ground bending up, three actuators shrinking like an inchworm, and a five-actuator inchworm robot, as in Fig. 1.

Our modeling is based on the Euler-Bernoulli small-amplitude model of displacement y versus the lateral position x . In such a model, for an actuator with a single applied voltage, the shape is determined by:

- 1) Piezoelectric effect: $d^2y/dx^2 = \gamma V$, where V is the applied voltage, and γ is a constant related with material properties. See Appendix VII-B for details.

Top View

(a)

Side View (When Actuated)

(b)

Figure 4. Robot setup: (a) top view; (b) side view when it is actuated. 5-actuator robot was put on an acrylic pad, wired to high voltage supplies with light and thin gold wires. The voltages can be controlled in real-time.

- 2) Distributed load q (mass per length): $d^4y/dx^4 = qg/EI$, where EI is the effective flexural rigidity of the trimorph structure (Appendix VII-B).
- 3) External vertical force F : $d^3y/dx^3 = F/EI$.
- 4) Discrete mass m : discontinuity in d^3y/dx^3 equals $-mg/EI$

The model must be applied piecewise because the actuator voltage changes from one section to another, and because in some sections the actuator is laying on the ground, so the ground is applying a vertical force on the actuator.

Regarding boundary conditions on the solutions:

- 1) dy/dx must always be continuous, including at all interfaces between different actuators.
- 2) Defining the flat ground as $y = 0$, y must be ≥ 0 (easily extended in more complex arrangements)
- 3) dy/dx must be continuous.
- 4) The ground must support the weight of the actuator - described through a "ground force" $F_{\text{Ground}}(x)$ acting on the robot described later, and
- 5) the total torque on an unconstrained robot about its center of mass must be zero.

We now apply this model to increasingly complicated shapes which underly the motion of our soft robot.

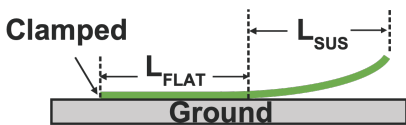


Figure 5. One-unit setup on the ground with the left end clamped. A negative voltage is applied to make the actuator unit bend up. One part of it (L_{SUS}) is suspended in the air, the other part (L_{FLAT}) lays flat on the ground due to gravity.

2) *Single actuator with one end clamped parallel to the ground* : Fig. 5 shows one actuator put on the ground with the left end clamped. When voltage is applied for it to bend up, part of it (L_{FLAT}) keeps flat on the ground, and the other part

(L_{SUS}) lifts up. So how can we analytically find the suspended length L_{SUS} ?

In the suspended region ($0 \leq x \leq L_{\text{SUS}}$), where the only force on the robot is gravity, with the piezoelectric effects and the boundary condition that $y(x) = 0$ and $dy/dx(x=0) = 0$, the shape is well known to be [28]:

$$y(x) = \frac{1}{2}\gamma V x^2 - \frac{qg}{24EI}x^2(x^2 - 4L_{\text{SUS}}x + 6L_{\text{SUS}}^2) \quad (1)$$

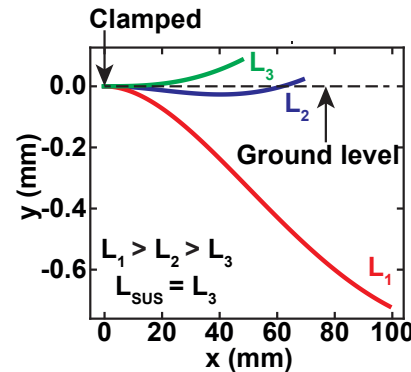
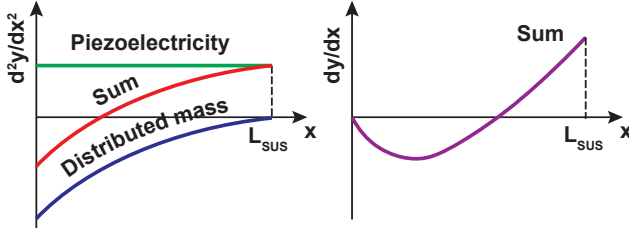


Figure 6. Plot of shape for an actuator curling up, with the left end clamped at $y = 0$ and $dy/dx = 0$. The self-consistent thought process of the model: the suspended length L_{SUS} would be the largest L (L_3) that make the result physical, i.e. all $y(x) > 0$.

A self-consistent approach demonstrated in Fig. 6 is proposed to solve L_{SUS} : for small L_{SUS} , we easily see that dy/dx is always ≥ 0 , so the suspended region is indeed suspended. For large L_{SUS} , we see y might go to negative at some x , which is not consistent with our assumption of an actuator off the ground. Thus, for any applied voltage, only a finite distance lifts off the ground. The region to the left of the "lift-off" part has $y = 0$ and $dy/dx = 0$.

We will look at the second derivatives to determine L_{SUS} . Fig. 7 shows the second derivative components caused by

Long Lsus: part of the actuator goes below the ground



Short Long Lsus: all of the actuator stays above the ground

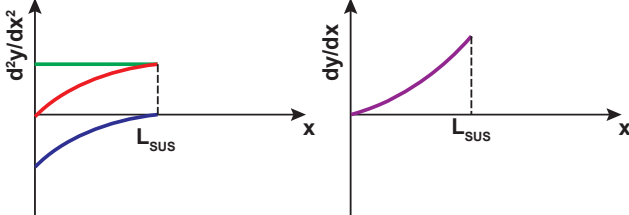


Figure 7. Second derivatives first derivatives of the shape caused by piezoelectricity, gravity, and the sum with different suspended lengths.

piezoelectricity, gravity, and the sum. Since the piezoelectricity d^2y_{piezo}/dx^2 is constant and the gravity d^2y_{mass}/dx^2 is monotonically increasing, when the lift-off length L_{SUS} is too long, the second derivative of the sum d^2y/dx^2 is negative at $x = 0$. So dy/dx will start to go negative when $x > 0$. Since $y(x = 0) = 0$, y will go negative as well. This result is not physical, as we assumed $y > 0$ everywhere due to the ground. By reducing the lift-off length, d^2y/dx^2 will increase. When $d^2y/dx^2(x = 0)$ reaches 0, dy/dx goes positive when $x > 0$, and the actuator will always be above ground. It means that L_{SUS} is the solution of $d^2y/dx^2(x = 0) = 0$. Therefore, we derived:

$$L_{\text{SUS}} = \sqrt{\frac{2EI}{qg}\gamma V} \quad (2)$$

Substitute Eq. (2) into Eq. (1), we can have $y(x)$ analytically. For the suspended portion:

$$y(x) = -\frac{qg}{24EI}x^4 + \frac{\sqrt{2}}{6}\sqrt{\frac{qg}{EI}\gamma V}x^3 \quad (3)$$

While for the other flat part, $y(x) = 0$.

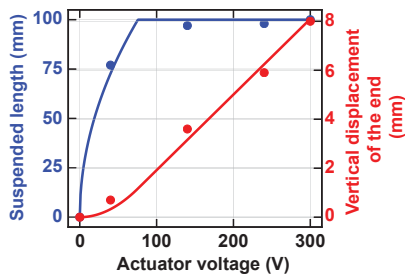


Figure 8. The suspended length L_{SUS} (blue) and displacement (red) of the free end versus the driving voltage for a single actuator with one end clamped parallel to the ground. Model (lines) and experimental measurements (points) show good matches.

Fig. 8 plots L_{SUS} and displacement at the end predicted from the model and the experimental measurements as a function of the actuator voltage. (Parameter values are listed in Appendix VII-A1.) Actuator shapes are detected by vision sensing, and L_{SUS} was exactly determined from the shape (extracted by plotting dy/dx v.s. x). Model and experiment show good agreement with no adjustable parameters.

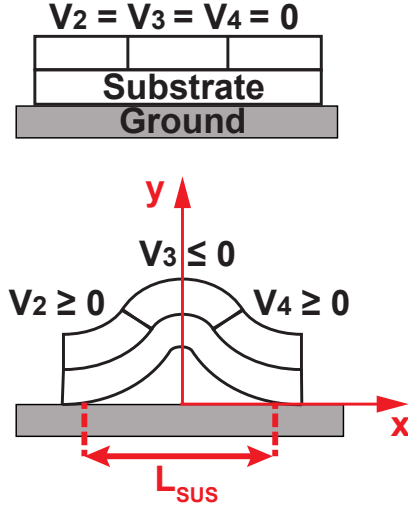


Figure 9. Three-actuator setup shrinks and lifts off with voltages applied.

3) *Three actuators curl up with symmetric voltages:* This subsection shows how the model predicts the shape of the middle three actuators (actuators #2 – #4) on the ground curling up with symmetric voltages applied. Fig. 9 shows the cross-section diagram of the setup: part of the setup would be flat on the ground; length of the total suspended part is L_{SUS} ; The applied voltages follow mirror symmetry ($V_2 = V_4 \geq 0$, $V_3 \leq 0$). Combining piezoelectricity with Euler-Bernoulli model, we get [28]:

$$y(x) = -\frac{1}{24}\frac{qg}{EI}x^4 + \frac{1}{2}a_2x^2 + Y(x) + a_0 \quad (4)$$

$Y(x)$ which results from piezoelectricity is:

$$Y(x) = \begin{cases} -\frac{1}{2}\gamma|V_3|x^2, & (-\frac{L}{2} \leq x \leq \frac{L}{2}) \\ \frac{1}{2}\gamma|V_4|x^2 - \frac{1}{2}\gamma(|V_3| + |V_4|)Lx + \frac{1}{8}\gamma(|V_3| + |V_4|)L^2, & (\frac{L}{2} \leq x \leq \frac{3L}{2}) \\ \frac{1}{2}\gamma|V_4|x^2 + \frac{1}{2}\gamma(|V_3| + |V_4|)Lx + \frac{1}{8}\gamma(|V_3| + |V_4|)L^2, & (-\frac{3L}{2} \leq x \leq -\frac{L}{2}) \end{cases} \quad (5)$$

The constants a_0 and a_2 can be solved from the boundary conditions $y(x = L_{\text{SUS}}/2) = 0$ and $dy/dx(x = L_{\text{SUS}}/2) = 0$:

$$a_0 = \frac{1}{384}\frac{qg}{EI}L_{\text{SUS}}^4 + \frac{1}{4}L_{\text{SUS}}dY/dx(x = L_{\text{SUS}}/2) - Y(x = L_{\text{SUS}}/2) \quad (6)$$

$$a_2 = \frac{1}{24}\frac{qg}{EI}L_{\text{SUS}}^2 - \frac{2dY/dx(x = L_{\text{SUS}}/2)}{L_{\text{SUS}}} \quad (7)$$

Similar with the analysis in Section III-B2 for single actuator, L_{SUS} satisfies $d^2y/dx^2(x = L_{\text{SUS}}/2) = 0$. Therefore, if $L_{\text{SUS}} \geq L$,

$$L_{\text{SUS}} = \sqrt[3]{12\gamma(|V_3| + |V_4|)L\frac{EI}{qg}} \quad (8)$$

If $L_{\text{SUS}} < L$, $L_{\text{SUS}} = 0$.

One thing to note is that the pick of L_{SUS} also need $y(0) \geq 0$, where

$$y(0) = -\frac{1}{384}\frac{qg}{EI}L_{\text{SUS}}^4 + \frac{1}{8}\gamma(|V_3| + |V_4|)L(L_{\text{SUS}} - L) \quad (9)$$

Therefore, L_{SUS} will be the minimum of (8) and the solution of (9). The setup's shape is derived by taking L_{SUS} into (4), combining (5) and (6).

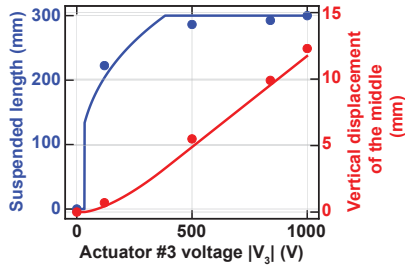


Figure 10. The suspended length L_{SUS} (blue) and displacement (red) of the end versus the driving voltage for the three-actuator setup, where $V_2 = V_4 = 0.3|V_3|$. Model (lines) and experimental measurements (points) show good matches.

Fig. 10 plots L_{SUS} and displacement at the end predicted from the model and the experimental measurements as a function of V_3 , and $V_2 = V_4 = 0.3|V_3|$. Shapes are detected by vision sensing, and L_{SUS} was extracted with the first derivatives. Model and experiment match well.

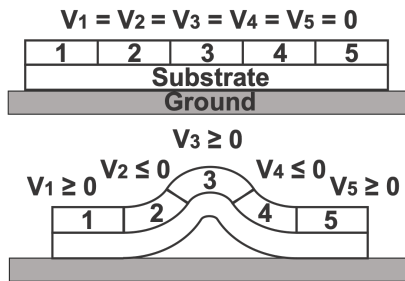


Figure 11. The five-unit robot prototype on the ground. With applying voltages, the middle three units shrink and lift off.

4) Five-actuator robot: Fig. 11 shows a cross-section sketch of such a robot. Actuators are numbered as #1 – #5 and voltages V_1 – V_5 are applied. Among the voltages, $V_1 \geq 0$, $V_5 \geq 0$, $V_2 = V_4 \geq 0$, and $V_3 \leq 0$.

There are two cases to analyze the robot's shape:

- When the voltages applied are low, the interfaces between actuators #1/#2 and #4/#5 are flat so that we can separate the analysis of the robot into three parts: Section III-B2 applies to actuator #1 and #5, and Section III-B3 applies to actuators #2 – #4.

- When the voltages applied are high enough, the flat regions approach zero such that only two points will touch the ground. Naturally, the robot cannot be separated as described previously, as we need to find where the points are. Let's say x_1 and x_2 are the positions of the points touching the ground. $x = 0$ is the most left end of the robot. The shape of the robot would be:

$$y(x) = \begin{cases} y_1(x) & 0 < x \leq x_1 \\ y_2(x) & x_1 < x \leq x_2 \\ y_3(x) & x_2 < x \leq 5L \end{cases} \quad (10)$$

And:

$$\begin{pmatrix} y_1(x) \\ y_2(x) \\ y_3(x) \end{pmatrix} = \begin{pmatrix} a_{01} \\ a_{02} \\ a_{03} \end{pmatrix} + \begin{pmatrix} a_{11} \\ a_{12} \\ a_{13} \end{pmatrix}x + \frac{1}{2} \begin{pmatrix} a_{21} \\ a_{22} \\ a_{23} \end{pmatrix}x^2 + \frac{1}{6} \begin{pmatrix} a_{31} \\ a_{32} \\ a_{33} \end{pmatrix}x^3 - \frac{1}{24} \frac{qg}{EI}x^4 + Y(x) \quad (11)$$

Combining with the boundary conditions: $y_1(x_1) = y_2(x_1) = 0$, $y'_1(x_1) = y'_2(x_1) = 0$, $y_2(x_2) = y_3(x_2) = 0$, $y'_2(x_2) = y'_3(x_2) = 0$, $y''(0) = Y''(0)$, $y'''(0) = 0$, $y''(5L) = Y''(5L)$, $y'''(5L) = 0$, $y''_1(x_1) = y''_2(x_1)$, $y''_2(x_2) = y''_3(x_2)$, the shape can then be solved numerically.

Fig. 12 shows the calculated numerical solution for $V_1 = 300$ V, $V_2 = 300$ V, $V_3 = -960$ V, $V_4 = 300$ V, and $V_5 = 300$ V. We found in the symmetric case that the single points that touch the ground are 8.1 mm to the right of the 1/2 interface (left of the 4/5 interface). For practical voltage limits on our piezoelectrics, these ground points did not deviate more than a few mm from the interfaces of the piezoelectric units. Thus one might approximate these locations as being at the interfaces.

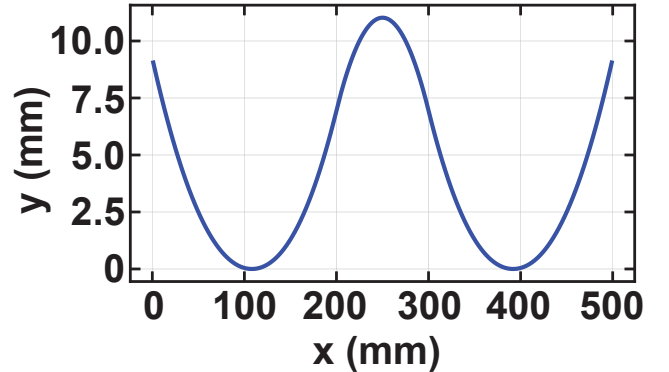


Figure 12. Numerical solution of the robot shape when $V_1 = 300$ V, $V_2 = 300$ V, $V_3 = -960$ V, $V_4 = 300$ V, and $V_5 = 300$ V. The single points that touch the ground are at $x = 108.1$ mm and $x = 391.9$ mm.

We then compare the model solution to the experiment, using voltages $V_1 = 300$ V, $V_2 = 300$ V, $V_3 = -960$ V, $V_4 = 300$ V, $V_5 = 0$ V. Fig. 13 shows robot shapes for different steps in a movement cycle as described in Section I. Vision sensing was implemented with three cameras, and the combined video

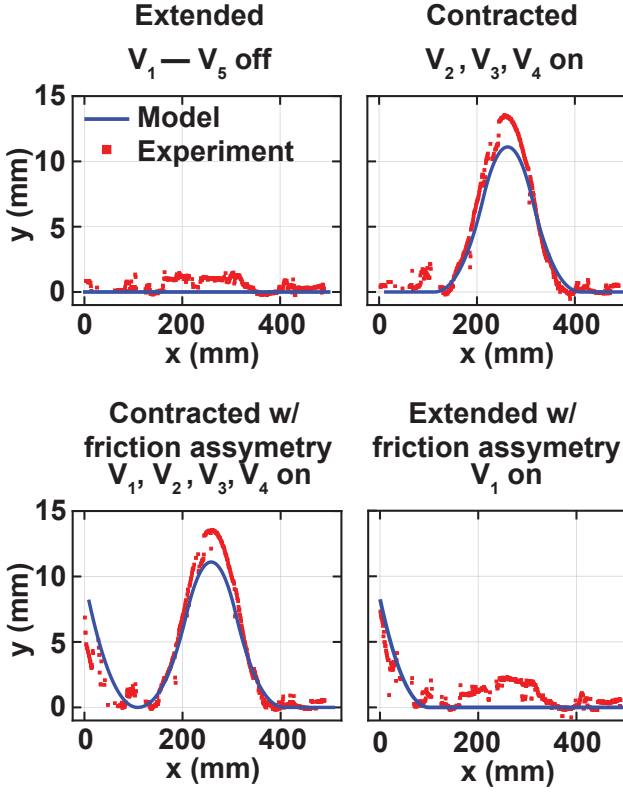


Figure 13. Robot shapes: model v.s. experiment for all steps in a movement cycle. Voltages: $V_1 = 300$ V, $V_2 = 300$ V, $V_3 = -960$ V, $V_4 = 300$ V, $V_5 = 0$ V.

from the cameras was used to extract the robot shape. $V_1 - V_5$ have different values, and different voltages turn on or off in different steps. Overall, the modeling results coming from first principles match the experimental measurement coming from vision sensing, and the small difference between them was probably brought by initial bending. When all voltages are turned off, ideally, the robot should be flat on the ground, while in reality, this robot curls up in its middle section around $x = 300$ mm also at the interface between actuators 1 and 2 around $x = 100$ mm. This is probably due to the initial built-in curvature not included in the model formulated during robot assembly and handling. When $V_2 - V_4$ are turned on, the middle three actuators crawl and lift off from the ground. The initial bending at $x = 100$ mm and $x = 300$ mm kicks in to make the real shape a little bit shifted from modeling predictions. Then when V_1 is applied, actuator #1 starts to lift off the ground. The last step in a cycle is that when $V_2 - V_4$ are turned off, only actuator #1 is lifted off from the ground while we can still see the curling up around $x = 300$ mm due to initial bending, as we described earlier.

Moreover, we ignored several practical effects during modeling. For example, the width of the substrate is 2.5 cm, but the piezo unit width is only 2.0 cm. Also, only part of the PZT element is active, while the other area is only for electrical and mechanical connections. The length of the active area is 8.5 cm, while the overall length is 10 cm, and the active width is 1.4 cm while the overall width is 2 cm. For example, one can show the “effective” stiffness EI is changed by the extra

amount of steel (in the y -direction) without an actuator on top of it is increased by 8%. The decrease of curvatures is an effect we ignore.

5) *Amount of motion:* The amount of motion can also be derived analytically. Since the substrate is steel foil in practice, its Young’s modulus is so high that its length could not be changed during robot operation. Therefore, the horizontal movement would be the difference of the integration of the length after and before the displacement.

When voltages V_1, V_2, V_3 , and V_4 are applied, the middle three actuators curl up, and the most left actuator lifts off. As of the analysis in Section III-C2, when V_2, V_3 and V_4 turn off, the middle three actuators will flatten. L_{tot} is the total curve length, and L_x is the length in the x -direction. The contract of the length in the x -direction is:

$$\begin{aligned} L_{x,\text{contract}} &= L_{\text{tot}} - L_x \\ &= \int \left(\sqrt{1 + \left(\frac{dy}{dx} \right)^2} - 1 \right) dx \\ &= 2 \int_0^{L_{\text{SUS}}/2} \left(\sqrt{1 + \left(\frac{dy}{dx} \right)^2} - 1 \right) dx \\ (\text{When } |dy/dx| \ll 1) &\approx 2 \int_0^{L_{\text{SUS}}/2} \left(\frac{1}{2} \left(\frac{dy}{dx} \right)^2 \right) dx \end{aligned} \quad (12)$$

Therefore, when $|dy/dx| \ll 1$:

$$\begin{aligned} L_{x,\text{contract}} &= (|V_3| + |V_4|) \gamma L^3 \sqrt[3]{(qg/EI)\gamma^2 L^2 (|V_3| + |V_4|)^2} \\ &+ \frac{33\sqrt{12}}{1120} (|V_3| + |V_4|)^2 \gamma^2 L^2 \\ &\sqrt[3]{(EI/qg)\gamma L (|V_3| + |V_4|)} \\ &- \frac{1}{12} \gamma^2 L^3 (|V_3| + |V_4|)^2 \\ &- \frac{1}{1920} \frac{qg}{EI} \gamma L^5 (|V_3| + |V_4|) \end{aligned} \quad (13)$$

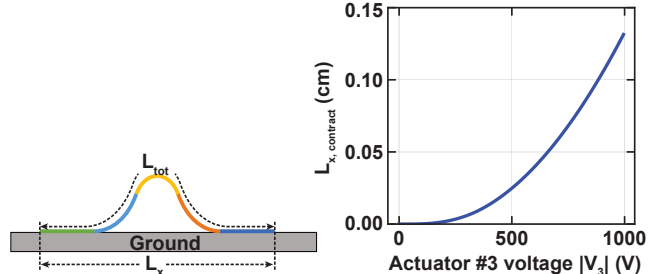


Figure 14. The contract of the length in the x direction $L_{x,\text{contract}} = L_{\text{tot}} - L_x$ versus the manitude of actuator #3 voltage V_3 , with $V_2 = V_4 = 0.3|V_3|$ and $V_5 = 0$ V. Monotonical increase of $L_{x,\text{contract}}$ with the voltage shows 0.15 cm movement at 1000 V.

Fig. 14 shows the relationship of the moving-in / moving-out amount $L_{x,\text{contract}}$ as a function of the magnitude of actuator #3 voltage $|V_3|$ ($V_3 \leq 0$), while $V_2 = V_4 = 0.3|V_3|$ and $V_5 = 0$ V. $L_{x,\text{contract}}$ increases monotonically with increasing

magnitude of V_3 and reaches about 1.3 mm when $|V_3| = 1000$ V.

C. Ground force analysis

1) *Ground force for a single actuator:* We modeled the shape of a single actuator with one end clamped parallel to the ground in Section III-B2. With its known shape, the ground force distribution can then be deduced by force balance. Fig. 15 shows its ground force distribution: for the part flat on the ground, the distributed ground force would equal the distributed load; for the part lift-off, as it does not touch the ground, the ground force would be zero; And there would also be a discrete ground force at the point that it starts to lift off, the magnitude equals the gravity of the suspended part.

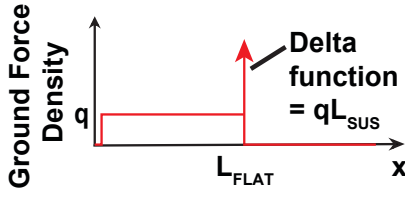


Figure 15. Ground force distribution of a single actuator with its left end clamped on the ground.

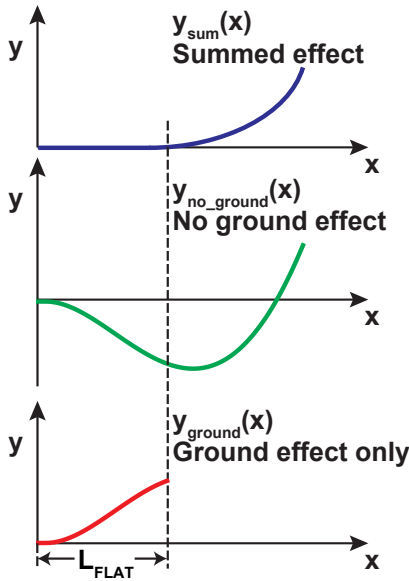


Figure 16. Actuator shape separating the effect of ground forces.

The ground force distribution can be deduced formally by separating gravity and ground force effects. Fig. 16 shows the final actuator shape ($y(x)$) with applied voltage and the one with only piezoelectricity and gravity ($y_{no_ground}(x)$). The difference ($y_{ground}(x)$) between them for the flat part reflects the effects of the ground force. For the flat part, we know $y_{sum}(x) = 0$, and if without ground force, the shape would be:

$$y_{no_ground}(x) = -\frac{qg}{24EI}x^4 + \frac{qgL}{6EI}x^3 + \left(\frac{1}{2}\kappa - \frac{qgL^2}{4EI}\right)x^2 \quad (14)$$

Therefore, the difference reflecting the ground force effects for the flat part ($0 \leq x \leq L_{FLAT}$) is:

$$y_{ground}(x) = y_{sum}(x) - y_{no_ground}(x) = \frac{qg}{24EI}x^4 - \frac{qgL}{6EI}x^3 + \left(\frac{qgL^2}{4EI} - \frac{1}{2}\kappa\right)x^2 \quad (15)$$

The shear force caused by the ground force is proportional to the third derivative of the displacement $y_{ground}(x)$:

$$F_{shear, ground}(x) = -EI \frac{d^3 y_{ground}}{dx^3} = qgL - qgx \quad (0 \leq x \leq L_{FLAT}) \quad (16)$$

And for the suspended part ($x > L_{FLAT}$):

$$F_{shear, ground}(x) = 0 \quad (x > L_{FLAT}) \quad (17)$$

Therefore, the distributed ground force is:

$$f_{ground}(x) = \begin{cases} qg + qgL_{SUS}\delta(x - L_{FLAT}) & (0 \leq x \leq L_{FLAT}) \\ 0 & (x > L_{FLAT}) \end{cases} \quad (18)$$

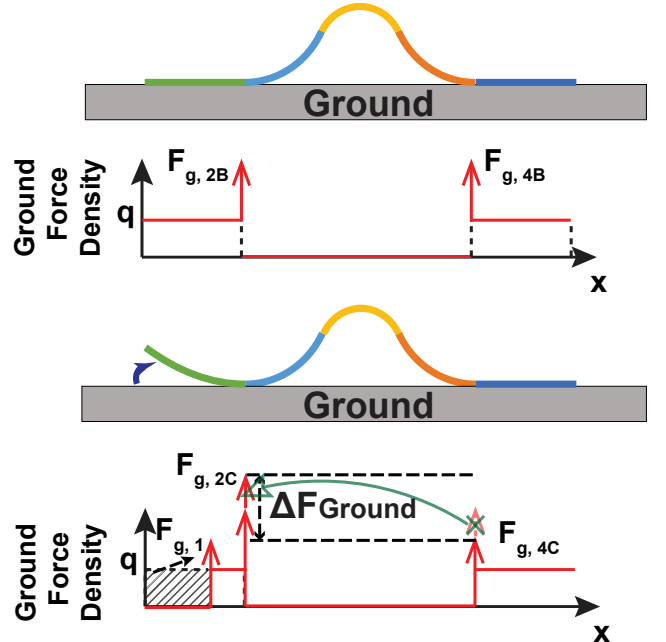


Figure 17. Mechanism of crawling: “seesaw” effect due to curving up of unit #1 leads to larger ground force on the left half part, and therefore the friction asymmetry.

2) *Ground force and friction asymmetry for the robot :* The key question this subsection answers is how to predict the robot’s motion and design the motion from the prediction. It turns out that the key to the movement is ground force and friction.

Fig. 17 shows the mechanism of ground force and friction asymmetry. When voltages V_2 V_3 and V_4 are applied, the middle three actuators curl up; Then V_1 is applied: the middle three actuators keep the same, but the most left actuator lifts off, and

because the ground force of actuator #1 moves inside ($F_{g,1}$), for torque balance, $F_{g,2}$ would increase ($F_{g,2C} > F_{g,2B}$) and $F_{g,4}$ would decrease ($F_{g,4C} < F_{g,4B}$), this difference ΔF_{Ground} will result in larger friction at the left side and therefore fix of the left part when actuator #2 – #4 flatten.

The difference in ground force can be calculated analytically. In step (b), we have:

$$F_{g,2B} = F_{g,4B} = \frac{1}{2}qgL_{\text{SUS,MID}} \quad (19)$$

where $L_{\text{SUS,MID}}$ is the suspended length for the middle three actuators. In step (c), as $F_{g,1} = qL_{\text{SUS,LEFT}}$, take the middle of actuator #3 as the reference position, from the torque balance, we have:

$$\begin{aligned} F_{g,1} &\left(\frac{5}{2}L - L_{\text{SUS,LEFT}} \right) + F_{g,2C} \frac{1}{2}L_{\text{SUS,MID}} \\ &= F_{g,4C} \frac{1}{2}L_{\text{SUS,MID}} + qgL_{\text{SUS,LEFT}} \left(\frac{5}{2}L - \frac{1}{2}L_{\text{SUS,LEFT}} \right) \end{aligned} \quad (20)$$

and

$$F_{g,2C} + F_{g,4C} = qgL_{\text{SUS,MID}} \quad (21)$$

Therefore,

$$F_{g,2C} = \frac{1}{2}qgL_{\text{SUS,MID}} + \frac{qgL_{\text{SUS,LEFT}}^2}{2L_{\text{SUS,MID}}} \quad (22)$$

$$F_{g,4C} = \frac{1}{2}qgL_{\text{SUS,MID}} - \frac{qgL_{\text{SUS,LEFT}}^2}{2L_{\text{SUS,MID}}} \quad (23)$$

$$\begin{aligned} \Delta F_{\text{Ground}} &:= F_{g,2C} - F_{g,4C} \\ &= \frac{qgL_{\text{SUS,LEFT}}^2}{L_{\text{SUS,MID}}} \end{aligned} \quad (24)$$

And:

$$\frac{\Delta F_{\text{Ground}}}{F_{g,R}} = \frac{2L_{\text{SUS,LEFT}}^2}{L_{\text{SUS,MID}}^2 + 2LL_{\text{SUS,MID}} - L_{\text{SUS,LEFT}}^2} \quad (25)$$

where $F_{g,R}$ is the total ground force on the right side.

From formula (25), say $L_{\text{SUS,MID}} = 30$ cm and $L_{\text{SUS,LEFT}} = 10$ cm in practice. $\Delta F_{\text{Ground}}/F_{g,R} = 14.29\%$. Since friction is proportional to the ground force ($f = \mu F_g$, where μ is friction coefficient, uniform across the ground), the friction on the left side will be 14.29% more than the other side.

By substituting $L_{\text{SUS,LEFT}}$ and $L_{\text{SUS,MID}}$ from equation (2) and (8), when $L_{\text{SUS,LEFT}} \leq L$ and $L_{\text{SUS,MID}} \leq 3L$, we get:

$$\begin{aligned} \frac{\Delta F_{\text{Ground}}}{F_{g,R}} &= 2\gamma V_1 / \left(\sqrt[3]{18(qg/EI)[\gamma L(V_2 + V_3)]^2} \right. \\ &\quad \left. + \sqrt{2(qg/EI)\gamma V_1}L - \gamma V_1 \right) \end{aligned} \quad (26)$$

Experiments are conducted to validate the ground force difference between two ends. Five identical scales were put in a line under the robot during driving. The five scales are next

to each other without gaps, and they cover all the bottom areas of the robot. This is to measure the ground force distribution for different robot postures.

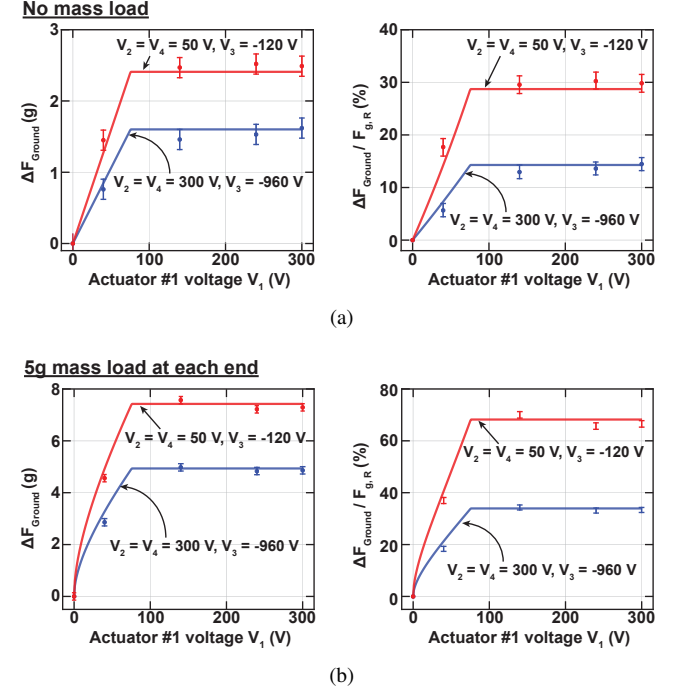


Figure 18. Ground force difference (ΔF_{Ground}) and the difference ratio ($\Delta F_{\text{Ground}}/F_{g,R}$) as a function of the voltage of the lifting end (actuator #1), for (a) no mass loads at the end; (b) 5g mass load at each end. This is in two cases: (i) $V_2 = 300$ V, $V_3 = -960$ V, $V_4 = 300$ V, $V_5 = 0$ V; and (ii) $V_2 = 50$ V, $V_3 = -120$ V, $V_4 = 50$ V, $V_5 = 0$ V. Error bars represent standard deviations.

Fig. 18a plots the ground force difference ratio as a function of voltage of the lifting actuator #1 comparing model and experiments, in two cases: (i) $V_2 = 300$ V, $V_3 = -960$ V, $V_4 = 300$ V, $V_5 = 0$ V; and (ii) $V_2 = 50$ V, $V_3 = -120$ V, $V_4 = 50$ V, $V_5 = 0$ V. Error bars represent standard deviations. Model and experiments match well. The ground force can be 30% more on the left end in the second case.

This number might be too small to overcome the surface variation. However, this asymmetry will be boosted when there are mass loads at both ends of the robot. When Δm heavy loads are placed on both ends of the robot, similarly we will have:

$$\Delta F_{\text{Ground}} = \frac{qgL_{\text{SUS,LEFT}}^2 + 2\Delta mgL_{\text{SUS,LEFT}}}{L_{\text{SUS,MID}}} \quad (27)$$

and

$$\begin{aligned} \frac{\Delta F_{\text{Ground}}}{F_{g,R}} &= [2L_{\text{SUS,LEFT}}^2 + 4\Delta mgL_{\text{SUS,LEFT}}/(qg)] \\ &\quad /(L_{\text{SUS,MID}}^2 + 2LL_{\text{SUS,MID}} + 2\Delta mL_{\text{SUS,MID}}/q \\ &\quad - L_{\text{SUS,LEFT}}^2 - 2\Delta mL_{\text{SUS,LEFT}}/q] \end{aligned}$$

Fig. 18b plots the ground force difference ratio for the same voltages with 5g mass load at each end of the robot. The difference is boosted to 70%.

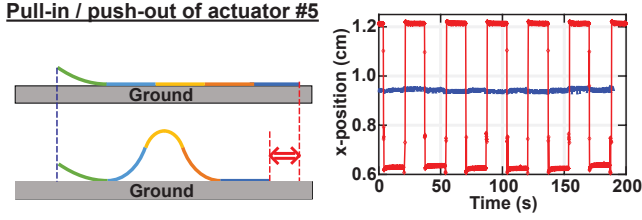


Figure 19. The horizontal position of the right end of actuator #5 (red) or the left end of actuator #1 (blue). One end moves in and out while the other end is holding the ground by lifting.

Fig. 19 shows the end of actuator #5 or actuator #1 moving in and out while the other end is holding the ground by lifting. The horizontal positions of the ends are plotted in the time domain, with multiple loops for robustness characterization. When V_1 is turned on, actuator #1 is lifted off from the ground. Because of the ground force asymmetry and friction asymmetry, this end will be held on the ground while $V_2 - V_4$ turns off (on) and the middle section of the robot is flattening (crawling).

The mechanism takes advantage of friction asymmetry due to gesture asymmetry in the steps. We validated that when one end lifts off, it will hold on the ground while the other end moves in or out, and how robust it is. Moreover, this mechanism can be further validated by taking off the gesture asymmetry to see whether or not the robot can move. There are two kinds of tests. The first one is that neither end lifts off, and the other is that they always lift off simultaneously. In both cases, the robot will always have symmetric voltage supplied and therefore symmetric displacements. Vision sensing tracks the position of the right end of actuator #5.

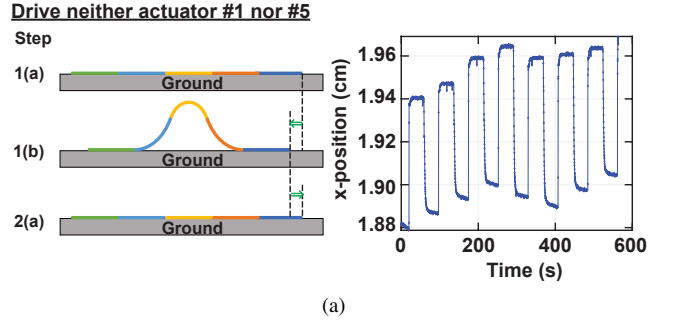
Fig. 20a shows the model demonstration and experimental result in the case neither actuator #1 nor #5 is driven. From step (c) to step (d), as of symmetry, when $V_2 - V_4$ are turned off, the target – the right end of actuator #5 – should be pushed forward by the same amount as pulling in from step (a) to step (b) so that the robot will not have net movement. Experimentally, the robot moves back and forth and almost has no net movement. The average movement is only $35\mu\text{m}$ per cycle forward.

Fig. 20b shows the case for driving actuators #1 and #5 simultaneously with the same voltages. From step (c) to step (d), as both actuators should bend up by the same amount, the predicted pushing-out and pulling-in movement of the target would be the same as well. Therefore, the robot would have no net motion. Vision sensing result matches the prediction, showing that the robot has a slight net forward movement, and the average is only $72.5\mu\text{m}$ per cycle.

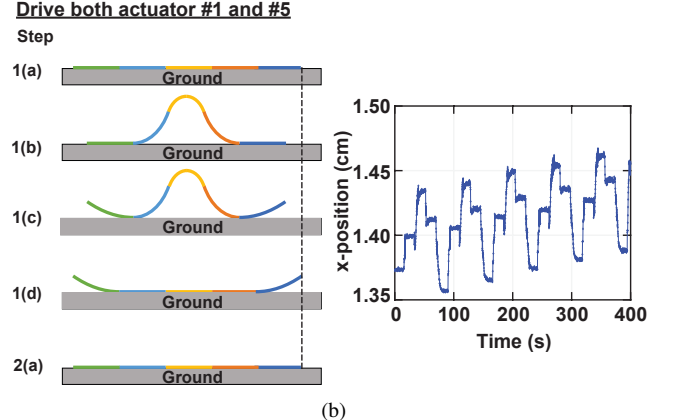
As analyzed later in Section IV-A, we can see that both the numbers are much smaller than the forward/backward motion per cycle.

IV. ROBOT INCHWORM MOTION

This section experimentally demonstrates the motion of the inchworm robot. Test results will be shown compared with model predictions – for forward motion, backward motion,



(a)



(b)

Figure 20. Motion mechanism validations – model predictions and experimental results for robot forward motion, in two cases: (a) drive neither actuator #1 nor #5; (b) drive both actuator #1 and #5.

payload carrying at different locations, and how motion speed scales with cycling frequencies.

A. Forward and backward motion

Fig. 21 shows the design of one cycle of its forward and backward motions in five steps per cycle with supplied voltages for each step.

For the forward motion:

- 1) V_5 is applied lifting up the right end to fix the right end on the ground by increasing its friction.
- 2) $V_2 - V_4$ are applied to make the middle three actuators crawl up, so the left end will move rightward.
- 3) V_5 turns off, and V_1 is applied to lift its left end and flatten the right end: the left part is holding on the surface.
- 4) The middle section flattens as $V_2 - V_4$ goes back to zero; since the left end is fixed, the robot has net forward motion compared with the previous cycle.

The backward motion is similar to the forward motion, but the sequence of the steps is reversed. The robot, by default, has a 25 g discrete payload each on interfaces of actuator #1/#2 and #4/#5 to compensate initial bending curvatures during assembly. The effect of this payload will be discussed in detail later in Section IV-C. It also carries a 5 g payload each on both ends to increase ground force difference, as discussed in Section III-C2.

Fig. 22a demonstrates the forward motion of the robot. V_1 to V_5 are 300 V, -1500 V, 300 V, 300 V and 300 V respectively.

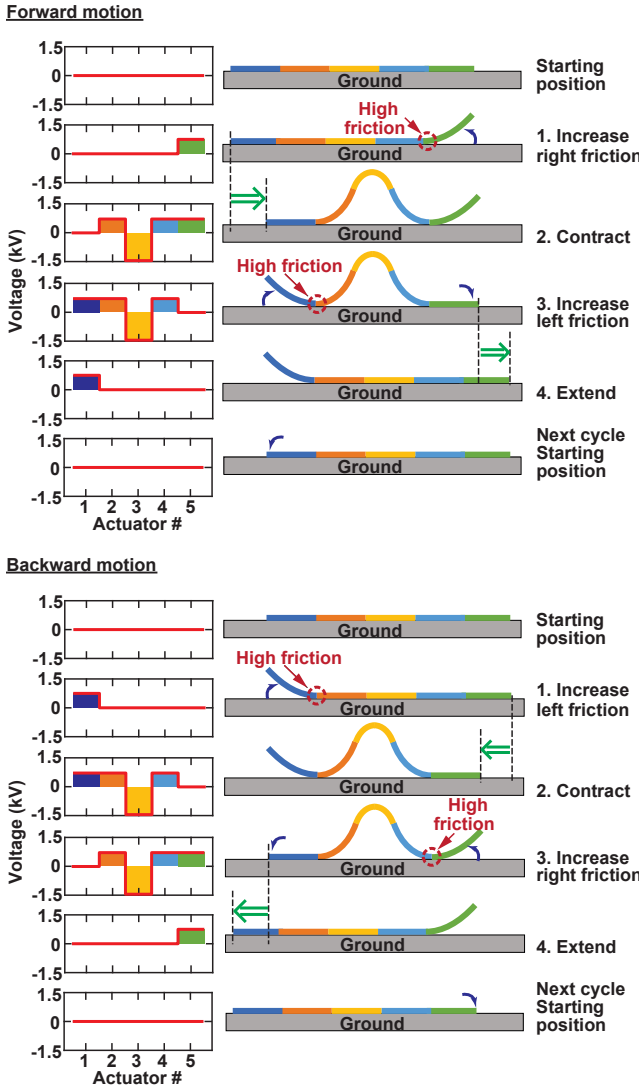


Figure 21. Robot motion design: one cycle of forward and backward motions in five steps with supplied voltages.

The robot is moving forward cycle by cycle, and each cycle takes 20 s as baseline tests. Faster cycles will be discussed later in Section IV-B. Vision sensing tracks the horizontal position of the end of actuator #1 in the time domain. Its value's increasing means that the target is moving forward, and vice versa. The robot moves 785 μm forward per cycle on average, and the average speed is 39 $\mu\text{m}/\text{second}$ forward for a 20-second cycle duration.

Fig. 22b shows the backward motion of the robot. It is similar to the forward motion, but the sequence of the steps is reversed. Therefore, the robot will move backward. As a result, the movement amount is similar: the robot moves 659 μm backward per cycle on average, and the average speed is 33 $\mu\text{m}/\text{second}$ backward with a 20-second cycle duration.

B. Movement scalability with driving speed

As the robot moves forward or backward cycle by cycle, its speed will depend on how fast we drive the robot. Since the model-predicted movement amount per cycle does not depend

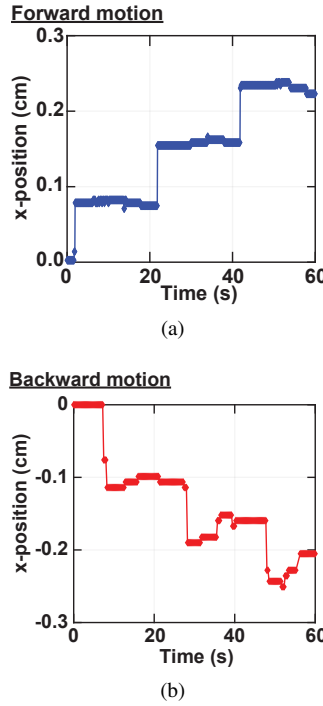


Figure 22. Inchworm motion of the robot. (a) The forward motion of the robot; (b) backward motion. The horizontal position of the end of actuator #5 is tracked in the time domain. $V_1 = 300 \text{ V}$, $V_2 = 300 \text{ V}$, $V_3 = -1500 \text{ V}$, $V_4 = 300 \text{ V}$, and $V_5 = 300 \text{ V}$. The robot is able to move 785 μm in average for each cycle of forward motion, and 659 μm for backward motion.

on cycle duration, the robot's speed should be proportional to the driving frequency.

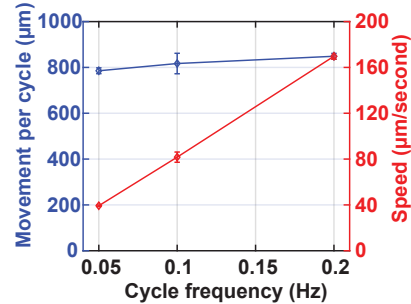


Figure 23. Robot inchworm movement scalability with driving frequency: the driving cycle duration changes from 20 s (0.05 Hz) to 5 s (0.2 Hz). The movement per cycle keeps almost constant while the average speed increases linearly with driving frequency.

Fig. 23 shows the experimental result of how the speed scales. The driving cycle duration changes from 20 s (0.05 Hz) to 5 s (0.2 Hz). The results match our prediction. The movement per cycle keeps almost constant as the cycle frequency changes, ranging from 785 μm per cycle to 848 μm per cycle. And the average speed increases linearly, from 39 $\mu\text{m}/\text{second}$ at cycle frequency 0.05 Hz to 170 $\mu\text{m}/\text{second}$ at 0.2 Hz.

The current limit of the speed is due to the bandwidth of the power converters since the power needed for the power converter would be proportional to the driving frequency, considering the 5V-to-1500V high voltage conversion ratio. With power converters enabling higher driving frequency such

as 2 Hz or 20 Hz, 10x or 100x speed might be achieved compared with 170 $\mu\text{m}/\text{second}$ driving at 0.2 Hz.

C. Movement with payload

In real applications, the robot perhaps carries not only the weight of itself but may also carry a payload. This part explores a payload's good locations and how much the robot can carry to move.

Several kinds of nuts with different sizes and weights are used as payload, and Apple Watches for real object carrying tests. Each watch is 37 g. The robot itself is 13 g heavy. There are two types of representative locations for loading. One is on the middle of actuator #3. When there is an object carried there, its gravity will make the robot bend less during driving, and therefore the movement will become less. The other is to simultaneously put the same weights at the interfaces between actuators #1 and #2 and #4/#5. When two objects with equivalent weights are put at these locations, as these sections never lift off from the ground even without load, their effects on the movement would be secondary. Therefore, carrying on these two locations can handle a much heavier load than the previous case. One thing that may affect the movement amount is increased friction on the ground as of the heavy load: imaging that if the friction is infinite, the middle section cannot lift off at all, and the robot cannot move.

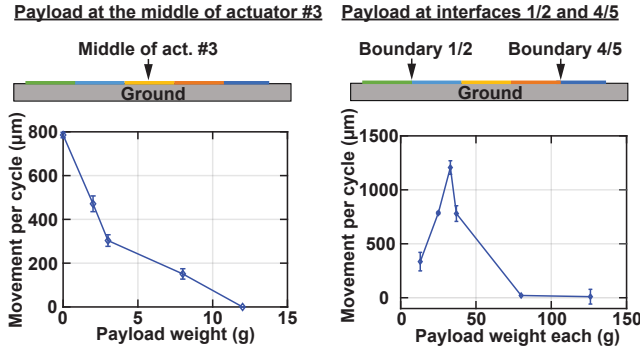


Figure 24. Payload effect: movement per cycle as a function of payload weight at each location for two different cases – at the middle of actuator #3 or at the interfaces 1/2 and 4/5.

Fig. 24 shows two locations on the robot carrying the payload and movement amount as a function of payload weights for both situations. When a load is put at the middle of actuator #3, with a 25 g constant payload at interfaces 1/2 and 4/5 and 5g at each end, the movement speed monotonically decreases with increasing payload until reaching zero at 12 g. For the other case, when two same loads are put on the two locations, the robot can carry up to 100 g for each weight (200 g in total), 16x heavier than the previous case and 15x heavier than its weight. Notably, when it carries two apple watches (74 g totally), 6x heavier than itself, it can move at a decent speed – 780 $\mu\text{m}/\text{cycle}$. Moreover, there is a sweet spot of movement when carrying 33 g for each weight (66 g in total) – 1207 $\mu\text{m}/\text{cycle}$. The sweet spot is probably because of the initial bending at the interface between actuators #1/#2 and #4/#5. It could affect the movement amount negatively, and it can be flattened with weight pressing on the top.

V. DISCUSSION

In this work, a soft robot was made in a scalable planar structure of an array of thin-film piezoelectric actuators. There are some previous recent research efforts on experimental demonstrations of piezoelectric soft robots, but not one with a scalable array. Examples include:

- a jumping cockroach robot with a single actuator [4],
- a robotic bee with flapping wings [5], and
- a robotic fish with a single actuator as its bending tail [6].

The scalable planar array structure opens a door for seamless integration of power, control, and sensing electronics by laminating these functional layers onto the robot [3]. This technique is called Large-Area Electronics (LAE). Devices such as transistors can be fabricated on soft and flexible foils using this technique [29], [30], [31]. In the past, it was used in flat panel displays, and now there is recent research work employing it in the areas such as sensing signal processing [32], [33] and wireless communications [34]. With such a technique and our current design, our robots will have the potential for full system integration as well as free and untethered operation.

VI. CONCLUSION

This paper designed and demonstrated a soft robot made of five electrically driven piezoelectric thin-film actuators. A soft body model was proposed and validated by experiments, combining gravity, piezoelectricity, and interactions with the ground (ground forces and frictions). Inchworm-inspired anchoring crawling motion was designed, explained by the model, and experimentally demonstrated. Crawling motion was caused by ground force difference, and therefore friction difference due to robot posture asymmetry. The robot can move forward and backward for 1.2 mm per cycle, carry payloads up to 200 g (16x robot weight) for moving.

This paper opens a door for a fastly responded and seamlessly integrated untethered soft robot for an undiscovered complicated environment. Future work includes performance optimization, control, and on-robot sensing development.

VII. APPENDIX

A. Notations and definitions

1) *Input material parameters*: The material parameters used in the model (Table I) are taken from the datasheet of the manufacturers, except the bonding epoxy thickness h_2 are measured experimentally.

2) *Other notations of the model*: Other notations of the model are shown in Table II.

B. Bending mechanism of the actuator

A single actuator consists of three layers: the top layer is a layer of PZT material, the middle layer is bonding epoxy, and the bottom layer is a substrate. This section talks about the bending mechanism of such an actuator and its design optimization.

Table I
INPUT MATERIAL PARAMETERS

Symbol	Description	Value	Measured (M) / Specified (S)
E_1	Young's modulus of the PZT unit	30 GPa	S
E_2	Young's modulus of the bonding epoxy	1.5 GPa	S
E_3	Young's modulus of the substrate	203 GPa	S
ρ_1	PZT unit density	3.2 g/cm ³	S
ρ_2	Epoxy density	1.1 g/cm ³	S
ρ_3	Steel substrate density	7.9 g/cm ³	S
h_1	Thickness of the PZT unit	300 μm	S
h_2	Thickness of the bonding epoxy	93 μm	M
h_3	Thickness of the substrate	50.8 μm	S
ν_1	Poisson ratio of the PZT unit	0.31	S
ν_3	Poisson ratio of the steel substrate	0.27	S
L	Length of a single actuator	10 cm	S
d_{pitch}	Electrode pitch distance	500 μm	S
$d_{31,1}$	Piezoelectric coefficient of the top layer PZT material	460 pm/V (for P1 actuators) 170 pm/V (for P2 actuators)	S
V	Voltage applied to the trimorph structure	-1500 V - +500V (for P1 actuators) -60 V - +360 V (for P2 actuators)	S
$V_1 - V_5$	Voltages applied to actuator #1 - #5	-1500 V - +500V (for P1 actuators) -60 V - +360 V (for P2 actuators)	S

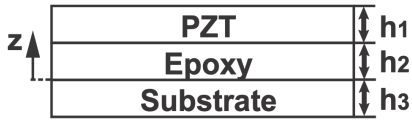


Figure 25. Cross-section sketch of the trimorph structure: piezoelectric layer PZT on the top, bonding epoxy in between and then substrate with thickness h_1 , h_2 and h_3 .

Fig. 25 shows the cross-section view of the trimorph structure, with PZT thickness h_1 , bonding epoxy thickness h_2 , and substrate thickness h_3 . When voltage is applied, the PZT tends to extend, but the substrate tends not to. The fighting between them would result in bending for the whole structure. The bending curvature is, referenced w.r.t. the neutral axis [35]:

$$\begin{aligned} \kappa &= \frac{1}{R} = z_1 E_1 h_1 d_{31,1} \epsilon_1 \frac{1}{EI} \\ &= \alpha V \frac{z_1 E_1 h_1}{EI} \\ &= \gamma V \end{aligned} \quad (28)$$

Table II
OTHER NOTATIONS OF THE MODEL

Symbol	Definition
q	Distributed mass of the robot per unit length
R	Bending radius of the trimorph structure
κ	Bending curvature of the trimorph structure
z_i	Position of the centerline w.r.t. the neural axis for the i-th layer
I_i	Second moment of area of the i-th layer w.r.t. its centerline
ϵ_1	Magnitude of the electric field in the PZT layer
EI	Effective flexural rigidity of the trimorph structure
α	Free-standing voltage expansion coefficient
γ	Bending curvature per unit voltage of the trimorph structure
L_{FLAT}	Length of the flat part of a single actuator setup
L_{SUS}	Length of the suspended part of a single actuator setup
$y_{\text{piezo}}(x)$, $y_{\text{mass}}(x)$	Displacement caused by piezoelectric effects and gravity
$y_{\text{sum}}(x)$	Displacement summing up all the effects
$y_{\text{no_ground}}(x)$	Displacement if there is no ground force
$y_{\text{ground}}(x)$	Displacement due to ground forces
$F_{\text{shear, ground}}(x)$	Shear force due to ground forces
$f_{\text{ground}}(x)$	Distributed ground force
$\kappa(x)$	$\gamma V(x)$, $V(x)$ is the voltage applied to each actuator
$\theta(x)$	$\int_0^x \kappa(x') dx'$
$Y(x)$	$\int_0^x \theta(x') dx'$
$F_{g,1}$	Discrete ground force on the lift-off point of actuator #1
$F_{g,2B}$	Discrete ground force on the lift-off point of actuator #2 in step (b)
$F_{g,4B}$	Discrete ground force on the lift-off point of actuator #4 in step (b)
$F_{g,2C}$	Discrete ground force on the lift-off point of actuator #2 in step (c)
$F_{g,4C}$	Discrete ground force on the lift-off point of actuator #4 in step (c)
ΔF_{Ground}	The difference of the ground force between the left and the right part
$L_{\text{SUS,LEFT}},$ $L_{\text{SUS,MID}}$	Lengths of suspended part of actuator #1 and the middle three actuators
x_{fixed}	Horizontal position of the fixed point
Δx	Horizontal movement during a cycle

where $\alpha = d_{31,1}/d_{\text{pitch}}$, $d_{31,1}$ is the piezoelectric constant of the 1st layer, d_{pitch} is the distance between the neighboring electrodes. z_i ($i = 1, 2, 3$) is the position of the centerline for each layer w.r.t. the neutral axis, E_i is Young's modulus for i-th layer, ϵ_1 is the magnitude of the electric field in the layer inducing piezoelectricity, EI is the flexural rigidity per unit width of the whole structure, α is the free-standing voltage expansion coefficient, V is the applied voltage, and γ is the bending curvature per unit voltage. We would have:

$$EI = \sum_{i=1}^3 E_i (I_i + h_i z_i^2) \quad (29)$$

where

$$I_i = \frac{1}{12} h_i^3 \quad (30)$$

And the position of the neutral axis will be:

$$z_N = \frac{\sum_i z_i E_i h_i}{\sum_i E_i h_i} \quad (31)$$

C. Model validation for a single-actuator cantilever

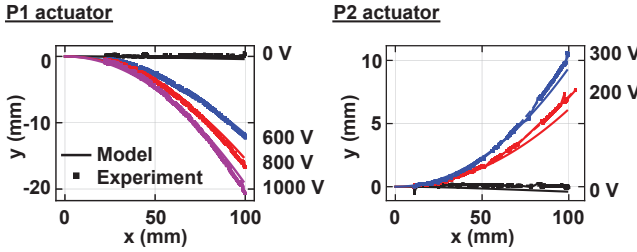


Figure 26. Model validation for single actuator cantilever settings. A single actuator is floated in the air, the top surface facing up, clamped on its left end. Both P1 actuators (a type of actuator that prefers to bend down) and P2 actuators (prefer to bend up) are tested.

Fig. 26 shows model validation in single actuator cantilever settings. A single actuator, as described in Section II, is floated in the air with its left end clamped. Two kinds of actuators we used on the robot will be tested here: one prefers to bend down (called “P1 actuator”), and the other prefers to bend up (called “P2 actuator”). In both scenarios, gravity will take into effect to pull the actuator down. The voltage ranges that they can take are also different. Vision sensing described in Section III-B4 is used to extract the shape of the actuators for different applied voltages. Each actuator is 10 cm long. A P1 actuator can bend down by about 2 cm with 1000 V supplied from a 5V-to-1500V power converter, and a P2 actuator can bend up by about 1 cm with 300 V applied. The experimental results all have good agreements with the modeling results.

D. Actuator performance optimization

Actuator’s bending performance is optimized by tuning the thickness of the substrate. If the substrate is too thin, it is very soft so that it would not bend but will extend together with the piezoelectric unit. If the substrate is too thick, it is too stiff to be bent by piezoelectricity. Therefore, there is a sweet spot of substrate thickness that optimizes the performance. This trade-off needs to be taken into considerations when designing the actuators.

Fig. 27 shows the bending curvature as a function of substrate thickness. The thickness of the bonding epoxy is measured experimentally, and all other material parameters are taken from commercially available products. The bending curvature reaches its maximum when the substrate thickness is 65 μ m. Therefore, the substrate thickness is picked to be 50 μ m, the nearest one to the optimal point commonly available.

REFERENCES

- [1] Michael T. Tolley, Robert F. Shepherd, Bobak Mosadegh, Kevin C. Galloway, Michael Wehner, Michael Karpelson, Robert J. Wood, and George M. Whitesides. A Resilient, Untethered Soft Robot. *Soft Robotics*, 1(3):213–223, sep 2014.
- [2] Timothy Duggan, Logan Horowitz, Asena Ulug, Emilie Baker, and Kirstin Petersen. Inchworm-Inspired Locomotion in Untethered Soft Robots. In *2019 2nd IEEE International Conference on Soft Robotics (RoboSoft)*, pages 200–205. IEEE, apr 2019.
- [3] Xiaobin Ji, Xinchang Liu, Vito Cacucciolo, Matthias Imboden, Yoan Civet, Alae El Haitami, Sophie Cantin, Yves Perriard, and Herbert Shea. An autonomous untethered fast soft robotic insect driven by low-voltage dielectric elastomer actuators. *Science Robotics*, 4(37):eaaz6451, dec 2019.
- [4] Yichuan Wu, Justin K. Yim, Jiaming Liang, Zhichun Shao, Mingjing Qi, Junwen Zhong, Zihao Luo, Xiaojun Yan, Min Zhang, Xiaohao Wang, Ronald S. Fearing, Robert J. Full, and Liwei Lin. Insect-scale fast moving and ultrarobust soft robot. *Science Robotics*, 4(32):eaax1594, jul 2019.
- [5] Noah T. Jafferis, E. Farrell Helbling, Michael Karpelson, and Robert J. Wood. Untethered flight of an insect-sized flapping-wing microscale aerial vehicle. *Nature*, 570(7762):491–495, jun 2019.
- [6] Robert K. Katzschmann, Andrew D. Marchese, and Daniela Rus. Hydraulic Autonomous Soft Robotic Fish for 3D Swimming. In *Springer Tracts in Advanced Robotics*, volume 109, pages 405–420. Springer, Cham, 2016.
- [7] Thierry Bujard, Francesco Giorgio-Serchi, and Gabriel D. Weymouth. A resonant squid-inspired robot unlocks biological propulsive efficiency. *Science Robotics*, 6(50):eabd2971, jan 2021.
- [8] Michael Wehner, Ryan L. Truby, Daniel J. Fitzgerald, Bobak Mosadegh, George M. Whitesides, Jennifer A. Lewis, and Robert J. Wood. An integrated design and fabrication strategy for entirely soft, autonomous robots. *Nature*, 536(7617):451–455, aug 2016.
- [9] Je-Sung Koh and Kyu-Jin Cho. Omega-Shaped Inchworm-Inspired Crawling Robot With Large-Index-and-Pitch (LIP) SMA Spring Actuators. *IEEE/ASME Transactions on Mechatronics*, 18(2):419–429, apr 2013.
- [10] Hassan Hussein Hariri, Gim Song Soh, Shaohui Foong, and Kristin Wood. Locomotion Study of a Standing Wave Driven Piezoelectric Miniature Robot for Bi-Directional Motion. *IEEE Transactions on Robotics*, 33(3):742–747, jun 2017.
- [11] Rongzhen Xie, Manjia Su, Yihong Zhang, Mingjun Li, Haifei Zhu, and Yisheng Guan. PISRob: A Pneumatic Soft Robot for Locomoting Like an Inchworm. In *2018 IEEE International Conference on Robotics and Automation (ICRA)*, pages 3448–3453. IEEE, may 2018.
- [12] Yichuan Wu, Kong Y. Ho, Kento Kariya, Renxiao Xu, Weihua Cai, Junwen Zhong, Yuan Ma, Min Zhang, Xiaohao Wang, and Liwei Lin. PRE-curved PVDF/PI unimorph structures for biomimetic soft crawling actuators. In *2018 IEEE Micro Electro Mechanical Systems (MEMS)*, volume 2018-Janua, pages 581–584. IEEE, jan 2018.
- [13] Hanqing Niu, Ruoyu Feng, Yuwei Xie, Bowen Jiang, Yongzhi Sheng, Yang Yu, Hexi Baoyin, and Xiangyuan Zeng. MagWorm: A Biomimetic Magnet Embedded Worm-Like Soft Robot. *Soft Robotics*, page soro.2019.0167, aug 2020.
- [14] Jianglong Guo, Chaoqun Xiang, Andrew Conn, and Jonathan Rossiter. All-Soft Skin-Like Structures for Robotic Locomotion and Transportation. *Soft Robotics*, 7(3):309–320, jun 2020.
- [15] Junwen Huang, Yu Liu, Yuxin Yang, Zhijun Zhou, Jie Mao, Tong Wu, Jun Liu, Qipeng Cai, Chaohua Peng, Yiting Xu, Birong Zeng, Weiang Luo, Guorong Chen, Conghui Yuan, and Lizong Dai. Electrically programmable adhesive hydrogels for climbing robots. *Science Robotics*, 6(53):eabe1858, apr 2021.
- [16] M. Calisti, G. Picardi, and C. Laschi. Fundamentals of soft robot locomotion. *Journal of The Royal Society Interface*, 14(130):20170101, may 2017.

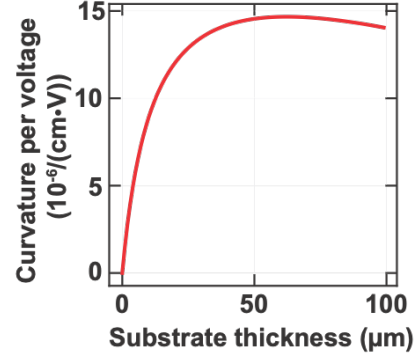


Figure 27. Actuator bending performance optimization: bending curvature as a function of substrate thickness.

- [17] Michael P. Murphy and Metin Sitti. Waalbot: An Agile Small-Scale Wall-Climbing Robot Utilizing Dry Elastomer Adhesives. *IEEE/ASME Transactions on Mechatronics*, 12(3):330–338, jun 2007.
- [18] Mihai Duduta, David R. Clarke, and Robert J. Wood. A high speed soft robot based on dielectric elastomer actuators. *Proceedings - IEEE International Conference on Robotics and Automation*, pages 4346–4351, jul 2017.
- [19] Huaxia Guo, Jinhua Zhang, Tao Wang, Yuanjie Li, Jun Hong, and Yue Li. Design and control of an inchworm-inspired soft robot with omega-arching locomotion. In *2017 IEEE International Conference on Robotics and Automation (ICRA)*, number c, pages 4154–4159. IEEE, may 2017.
- [20] W K Wilkie. NASA MFC piezocomposites: A development history. In *Proceedings of ISMA*, volume 2014, 2005.
- [21] Robert J. Webster and Bryan A. Jones. Design and kinematic modeling of constant curvature continuum robots: A review. *International Journal of Robotics Research*, 29(13):1661–1683, 2010.
- [22] Valentin Falkenhahn, Alexander Hildebrandt, Rudiger Neumann, and Oliver Sawodny. Model-based feedforward position control of constant curvature continuum robots using feedback linearization. In *2015 IEEE International Conference on Robotics and Automation (ICRA)*, volume 2015-June, pages 762–767. IEEE, may 2015.
- [23] Cosimo Della Santina, Antonio Bicchi, and Daniela Rus. On an Improved State Parametrization for Soft Robots With Piecewise Constant Curvature and Its Use in Model Based Control. *IEEE Robotics and Automation Letters*, 5(2):1001–1008, apr 2020.
- [24] N. Lobontiu, M. Goldfarb, and E. Garcia. A piezoelectric-driven inch-worm locomotion device. *Mechanism and Machine Theory*, 36(4):425–443, apr 2001.
- [25] Dibakar Bandopadhyaya. Derivation of Transfer Function of an IPMC Actuator Based on Pseudo-Rigid Body Model. *Journal of Reinforced Plastics and Composites*, 29(3):372–390, feb 2010.
- [26] Wen-Bo Li, Wen-Ming Zhang, Hong-Xiang Zou, Zhi-Ke Peng, and Guang Meng. A Fast Rolling Soft Robot Driven by Dielectric Elastomer. *IEEE/ASME Transactions on Mechatronics*, 23(4):1630–1640, aug 2018.
- [27] Bryan A. Jones, Ricky L. Gray, and Krishna Turlapati. Three dimensional statics for continuum robotics. In *2009 IEEE/RSJ International Conference on Intelligent Robots and Systems*, pages 2659–2664. IEEE, oct 2009.
- [28] Sung Jin Kim and James D. Jones. Influence of Piezo-Actuator Thickness on the Active Vibration Control of a Cantilever Beam. *Journal of Intelligent Material Systems and Structures*, 6(5):610–623, 1995.
- [29] Yasmin Afsar, Jenny Tang, Warren Rieutort-Louis, Liechao Huang, Yingzhe Hu, Josue Sanz-Robinson, Naveen Verma, Sigurd Wagner, and James C. Sturm. Impact of bending on flexible metal oxide TFTs and oscillator circuits. *Journal of the Society for Information Display*, 24(6):371–380, jun 2016.
- [30] Yoni Mehlman, Can Wu, Sigurd Wagner, Naveen Verma, and James C. Sturm. Gigahertz Zinc-Oxide TFT-Based Oscillators. *Device Research Conference - Conference Digest, DRC*, 2019-June:63–64, jun 2019.
- [31] Zhiwu Zheng, Levent E. Aygun, Yoni Mehlman, Sigurd Wagner, Naveen Verma, and James C. Sturm. Analyzing and Increasing Yield of ZnO Thin-Film Transistors for Large-area Sensing Systems by Preventing Process-Induced Gate Dielectric Breakdown. In *2019 Device Research Conference (DRC)*, volume 2019-June, pages 141–142. IEEE, jun 2019.
- [32] Yasmin Afsar, Tiffany Moy, Nicholas Brady, Sigurd Wagner, James C. Sturm, and Naveen Verma. Large-scale acquisition of large-area sensors using an array of frequency-hopping ZnO thin-film-transistor oscillators. *Digest of Technical Papers - IEEE International Solid-State Circuits Conference*, 60:256–257, mar 2017.
- [33] Levent E. Aygun, Prakhar Kumar, Zhiwu Zheng, Ting-Sheng Chen, Sigurd Wagner, James C. Sturm, and Naveen Verma. Hybrid LAE-CMOS Force-Sensing System Employing TFT-Based Compressed Sensing for Scalability of Tactile Sensing Skins. *IEEE Transactions on Biomedical Circuits and Systems*, 13(6):1264–1276, dec 2019.
- [34] Can Wu, Yue Ma, Suresh Venkatesh, Yoni Mehlman, Sigurd Wagner, James C. Sturm, and Naveen Verma. Gigahertz large-area-electronics RF switch and its application to reconfigurable antennas. *Technical Digest - International Electron Devices Meeting, IEDM*, 2020-Decem:33.6.1–33.6.4, dec 2020.
- [35] M.S. Weinberg. Working equations for piezoelectric actuators and sensors. *Journal of Microelectromechanical Systems*, 8(4):529–533, 1999.